

Morphology-dependent photocatalytic H₂-production activity of CdSJiaguo Yu^{a,*}, Yanfang Yu^a, Peng Zhou^a, Wei Xiao^{b,**}, Bei Cheng^a^a State Key Laboratory of Advanced Technology for Material Synthesis and Processing, Wuhan University of Technology, Luoshi Road 122#, Wuhan 430070, PR China^b School of Resource & Environmental Sciences, Wuhan University, Wuhan 430072, PR China

ARTICLE INFO

Article history:

Received 29 January 2014

Received in revised form 2 March 2014

Accepted 9 March 2014

Available online 18 March 2014

Keywords:

Photocatalyst

CdS

Hydrogen production

Solvent

Microstructure

ABSTRACT

Various morphologies of CdS photocatalysts, including nanoparticles, nanorods, urchin-like shape and nanowires were prepared via a solvothermal process by tailoring the solvent. Based on both experimental and theoretical simulation investigation, the microstructure evolution mechanism was specified. Visible-light-driven photocatalytic activities for hydrogen production over the different CdS products were compared and rationalized. CdS nanowires prepared with the utilization of tetraethylenepentamine (TEPA) as solvent and L-cysteine as sulfur precursor displayed excellent photocatalytic H₂-production activity of 803 $\mu\text{mol h}^{-1}$ with quantum efficiency (QE) of 37.7% at 420 nm. The enhanced photocatalytic activity was ascribed to the high purity, good crystallinity, and unique microstructure and band structure, which was favorable for transfer of photogenerated carriers and thus reduced the recombination of electron–hole pairs. This work showed that the nature of solvent had significant influence on the photocatalytic H₂-production activity of CdS, which adds knowledge on designing photocatalysts for visible-light-driven photocatalytic hydrogen evolution.

© 2014 Elsevier B.V. All rights reserved.

1. Introduction

Photocatalytic hydrogen evolution through water splitting on semiconductor photocatalysts is of great interest due to its intriguing application on converting renewable solar energy into storable chemical energy [1–11]. Among various semiconductor photocatalysts, TiO₂ photocatalysts possess excellent activity and stability, but require ultraviolet (UV) irradiation (about 4% of the solar spectrum) for effective photocatalysis, which severely limits its practical applications [12–15]. Alternatively, considerable efforts have been focused on developing visible-light-driven photocatalysts, capable of using abundant visible light ($\lambda \geq 420$ nm) accounting for about 43% of the solar spectrum. Metal sulfides are regarded as good candidates for visible-light photocatalysts. Among them, CdS has been intensively studied because its band-gap (2.4 eV) corresponds well with the spectrum of sunlight and the conduction band edge is more negative than H⁺/H₂ redox potential [16,17].

It was reported that photo-driven hydrogen evolution activity of CdS is highly dependent on its morphology, crystal structure,

crystallinity and particle size [18]. These factors directly influence the band gap structure and electron transfer processes, including charge separation, transport of the photogenerated carriers, and photochemical reaction at the photocatalyst/electrolyte interface. Up to now, numerous methods have been explored to fabricate CdS nanocrystals with different morphologies, such as micro/nano leaves [19], nanoporous nanosheets and hollow nanorods [20], hollow microrods [21], multi-armed nanorods [22], nanosteps [23], and microtowers [24]. In particular, one-dimensional (1D) CdS nanostructure has received considerable attention because the unique 1D structure could facilitate the electron transfer processes. There have been many reports on the synthesis of 1D CdS nanostructure with various approaches such as vapor–liquid–solid (VLS)-assisted method [25], colloidal micellar method [26], thermal evaporation [27], chemical vapor deposition [28], electrochemical deposition [29], hydrothermal [30], and solvothermal method [31]. Among these approaches, solvothermal method is one of the ideal industrial methods for its low cost and maneuverability. The 1D CdS nanostructures were synthesized in ethylenediamine or other amines as a single solvent or a mixture of solvents up to now. For example, Jang et al. [32] reported the solvothermal synthesis of CdS nanowires at different temperatures and time for photocatalytic hydrogen production. Li et al. [30] investigated the formation of CdS nanorods via a hydrothermal route with different molar ratios of ethylenediamine to Cd²⁺. Previous work has indicated that activities of bare CdS photocatalyst were mainly determined by the

* Corresponding author. Tel.: +86 27 87871029; fax: +86 27 87879468.

** Corresponding author. Tel.: +86 27 68775799; fax: +86 27 68775799.

E-mail addresses: jiaguoyu@yahoo.com (J. Yu), gabrielxiao@whu.edu.cn (W. Xiao).

Table 1

Preparation conditions, morphologies and physicochemical properties of the samples obtained from the sulfur source-dependent preparation.

Sample	Sulfur source	Solvent	Morphology	S_{BET} ($\text{m}^2 \text{g}^{-1}$)	QE (%)
S1	Thiourea	Ethylenediamine (EDA)	Nanorods	47	26.6
S2	TAA	Ethylenediamine (EDA)	Nanowires	19	27.6
S3	L-cysteine	Ethylenediamine (EDA)	Urchin-like	27	33.9
H1	thiourea	Distilled water	Cauliflower-like	5	0
H2	TAA	Distilled water	Nanoparticles	22	6.9
H3	L-cysteine	Distilled water	Hollow spheres	25	8.8

materials-related characteristics, with good activities occurring in samples with hexagonal crystal structure, good crystallinity and large surface area, short bulk-to-surface diffusion distance for photogenerated electrons and holes, and monodisperse noble metal as co-catalyst. Therefore, there is a large room for a further improvement of the photocatalytic activity of pure CdS by controlling the morphology.

However, to the best of our knowledge, the effect of nature of solvent on the microstructure and photocatalytic hydrogen production of CdS photocatalysts remains unexplored yet. In the present paper, we report a solvothermal synthesis of the morphology-controlled CdS photocatalysts by adjusting the sulfur source and solvent. Their activities for photocatalytic hydrogen evolution were evaluated using aqueous solution containing lactic acid as sacrificial reagent and Pt as co-catalyst under visible light irradiation. The formation mechanism and influence of different morphologies and the nature of solvents on the activity were also investigated and rationalized, based on both experimental and theoretical simulation investigation.

2. Experimental details

2.1. Sample preparation

All the reagents were of analytical grade and were used without further purification. Distilled water was used in all experiments. In a typical synthesis, 2 mmol cadmium acetate $\text{Cd}(\text{Ac})_2 \cdot 2\text{H}_2\text{O}$ and 4 mmol L-cysteine ($\text{C}_3\text{H}_7\text{NO}_2\text{S}$) were added into a 100 mL Teflon-lined autoclave which was filled with 50 mL ethylenediamine (EDA) as solvent. After stirring for 30 min, the autoclave was sealed and maintained at 180°C for 24 h. After the reaction, the autoclave cooled to room temperature naturally. The resulting precipitates were collected and washed thoroughly with distilled water and absolute ethanol several times. The final products were dried in vacuum at 60°C for 10 h. To investigate the effect of sulfur source on the crystal structure, morphology and photocatalytic performance of CdS photocatalysts, similar experiments were carried out using different sulfur sources, such as thiourea and thioacetamide (TAA) in the presence of EDA solution. Moreover, to investigate the effect of solvents on the crystal structure, morphology and photocatalytic performance of CdS photocatalysts, similar experiments were also carried out using tetraethylenepentamine (TEPA), diethylenetriamine (DETA), dodecylamine (DDA) and triethanolamine (TEA) as alternative solvents with sulfur source unchanged (L-cysteine). Tables 1 and 2 summarize the experimental conditions used in this work.

Table 2

Preparation conditions, morphologies and physicochemical properties of samples obtained from the solvent-dependent synthesis.

Sample	Sulfur source	Solvent	Morphology	S_{BET} ($\text{m}^2 \text{g}^{-1}$)	QE (%)
A	L-cysteine	Triethanolamine (TEA)	Irregular	61	0.5
B	L-cysteine	Dodecylamine (DDA)	Nanoparticles	34	20.2
C	L-cysteine	Diethylenetriamine (DETA)	Nanorods	41	21.2
D	L-cysteine	Ethylenediamine (EDA)	Urchin-like	27	33.9
E	L-cysteine	Tetraethylenepentamine (TEPA)	Nanowires	40	37.7

2.2. Characterizations

X-ray diffraction (XRD) patterns were obtained on a D/Max-RB X-ray diffractometer (Rigaku, Japan) with Cu $\text{K}\alpha$ irradiation at a scan rate (2θ) of 0.05°s^{-1} . The accelerating voltage and the applied current were 40 kV and 80 mA, respectively. The morphology was observed using a S-4800 Field Emission Scanning Electron Microscopy (FESEM, Hitachi, Japan) at an accelerating voltage of 5 kV. Elemental analysis was conducted on an Oxford Instruments X-ray analysis system attached to the FESEM. Transmission electron microscopy (TEM) and high-resolution transmission electron microscopy (HRTEM) analysis were conducted using a JEM-2100F electron microscope (JEOL, Japan) at an accelerating voltage of 200 kV. The BET surface areas (S_{BET}) of the samples were analyzed by nitrogen adsorption using a Micromeritics ASAP 2020 nitrogen adsorption apparatus (USA). All powdered samples were degassed at 150°C prior to nitrogen adsorption measurements. The BET surface areas were determined by a multipoint BET method using adsorption data in the relative pressure (P/P_0) range of 0.05–0.25. Desorption data were used to determine the pore size distribution by the Barret–Joyner–Halender (BJH) method, assuming a cylindrical pore model. X-ray photoelectron spectroscopy (XPS) measurements were done on a VG ESCALAB MKII XPS system with Mg $\text{K}\alpha$ source and a charge neutralizer. All the binding energies were referenced to the C 1s peak at 285.0 eV of the surface adventitious carbon. UV–vis diffuse reflectance spectra (UV–vis DRS) of the as-prepared samples were obtained on a UV–visible spectrophotometer (UV-2550, Shimadzu, Japan). BaSO_4 was used as a reflectance standard in a UV–vis diffuse reflectance experiment.

2.3. Photocatalytic hydrogen production

The photocatalytic hydrogen production experiments were performed in a 100 mL Pyrex flask at ambient temperature and atmospheric pressure, and openings of the flask were sealed with silicone rubber septum. A 350 W Xe arc lamp through a UV-cutoff filter ($\leq 420 \text{ nm}$) positioned 5 cm in front of the photocatalytic reactor was used as visible-light source (22 cm far away from the photocatalytic reactor). The focused intensity on the flask measured by a visible-light radiometer (Model: FZ-A, China) was ca. 150 mW cm^{-2} in the wavelength range of 420–1000 nm. In a typical photocatalytic experiment, 50 mg of catalyst was suspended in 80 mL mixed solution of lactic acid (8 mL) and water (72 mL) under magnetic stirring and a side-irradiation. Besides, a certain amount of $\text{H}_2\text{PtCl}_6 \cdot 6\text{H}_2\text{O}$ aqueous solution was dripped into the system to load Pt onto the surface of the photocatalyst by a photochemical

reduction deposition method. Before irradiation, the suspensions were bubbled by nitrogen for 40 min to remove the dissolved oxygen and to ensure that the reaction system is under anaerobic conditions. A continuous magnetic stirrer was applied at the bottom of the reactor in order to keep the photocatalyst particles in suspension state during the whole experiment. 0.4 mL of gas was intermittently sampled through the septum, and hydrogen concentration was analyzed by a gas chromatograph (GC-14C, Shimadzu, Japan, TCD, nitrogen as a carrier gas and 5 Å molecular sieve column). All glassware was carefully rinsed with distilled water prior to use. The apparent quantum efficiency (QE) was also measured under the same photocatalytic reaction conditions except that the light source was different. Four LED (3 W, 420 nm, Shenzhen LAMP-PLIC Science Co. Ltd. China), positioned 1 cm away from the reactor in four different direction, were used as light sources to trigger the photocatalytic reaction. The focused intensity and areas on the flask for each LED were ca. 6.0 mW cm^{-2} and 1 cm^2 , respectively. The QE was calculated according to Eq. (1):

$$\text{QE [\%]} = \frac{\text{number of reacted electron}}{\text{number of incident photons}} \times 100$$

$$= \frac{\text{number of evolved } \text{H}_2 \text{ molecules} \times 2}{\text{number of incident photons}} \times 100 \quad (1)$$

2.4. Computational details

Density functional theory (DFT) calculation is conducted by CASTEP (Cambridge Sequential Total Energy Package) based on the plane-wave-pseudo-potential approach. The exchange-correlation function adopts the Perdew–Burke–Ernzerhof (PBE) of the generalized gradient approximation (GGA). The ultrasoft pseudopotential is used to describe the interaction between valence electrons and the ionic core. Before building the model of CdS surface, the unit cell of hexagonal CdS was optimized with the cutoff energy of 350 eV and the Monkhorst-Pack k-point mesh of $7 \times 7 \times 4$. Then four repeating Cd–S layers were used to simulate the (100) and (001) surfaces of CdS, respectively. The interaction between adjacent atom slabs was eliminated by the vacuum slab with thickness of 15 Å. The cutoff energy of 350 eV and the Monkhorst-Pack k-point mesh of $7 \times 7 \times 1$ were used to optimize the geometry structures of (100) and (001) surfaces. The tolerances of energy, force, stress and displacement in the optimized calculation were $1.0 \times 10^{-5} \text{ eV}$ per atom, 0.03 eV Å^{-1} , 0.05 GPa and 0.001 Å , respectively. During the optimization calculations, the positions of all atoms except those in the bottom of the atom slabs were optimized. Moreover, the accuracy test was done. The obtained results suggested that no

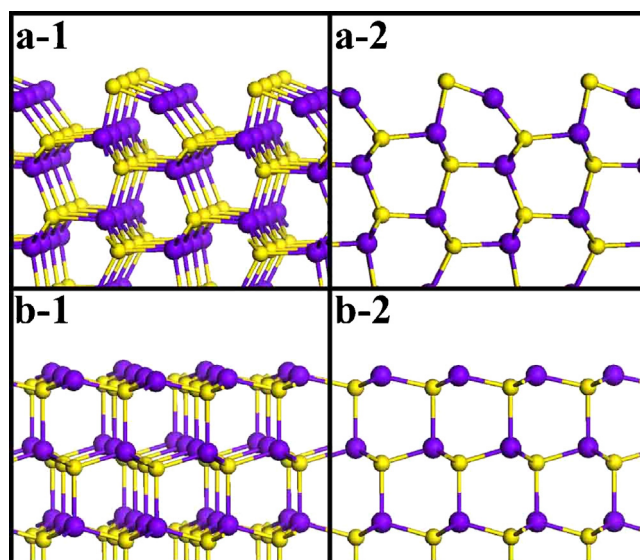


Fig. 1. The optimized (100) and (001) surfaces of hexagonal CdS: the side view (a-1) and front view (a-2) of (100) surface and the side view (b-1) and front view (b-2) of (001) surface. The yellow and purple spheres represent S and Cd atoms, respectively (For interpretation of the references to color in this figure legend, the reader is referred to the web version of this article.)

obvious variation was found in the displacement and energy, indicating the reliability of present calculation. The obtained geometry structures of (100) and (001) surfaces are shown in Fig. 1. It is clear that the Cd and S atoms both are exposed in the outmost layer of (100) and (001) surface.

3. Results and discussion

3.1. Morphology

Sulfur source-dependent preparation was firstly performed with either ethylenediamine (EDA) or water as solvents, aiming to specifying the optimal sulfur source in the following solvent dependent synthesis. As shown in Fig. 2a–c, nanorods, nanowires and urchin-like shape were obtained when thiourea, TAA and L-cysteine were used as sulfur source in the presence of ethylenediamine (EDA) solution, respectively. For comparison, the samples were prepared with the change of sulfur sources in distilled water. In the presence of distilled water, CdS cauliflower-like shape,

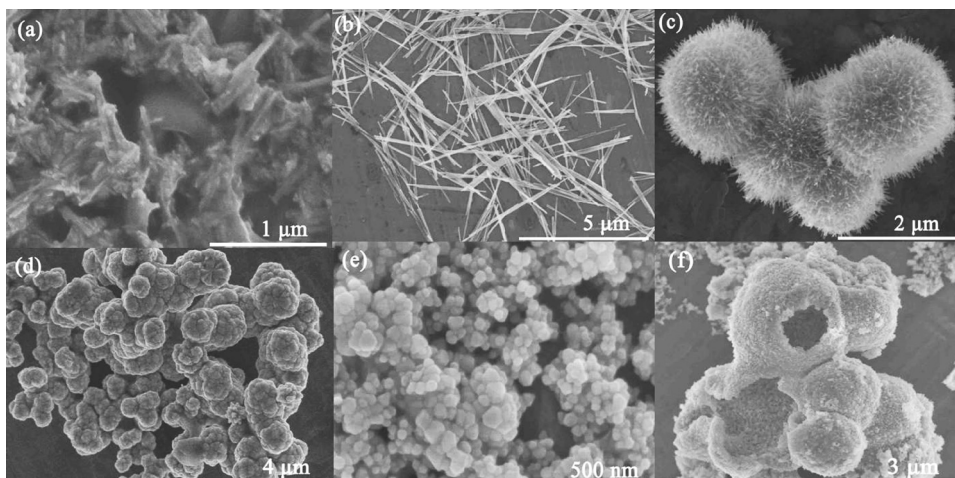


Fig. 2. FESEM images of samples S1 (a), S2 (b), S3 (c), H1 (d), H2 (e) and H3 (f).

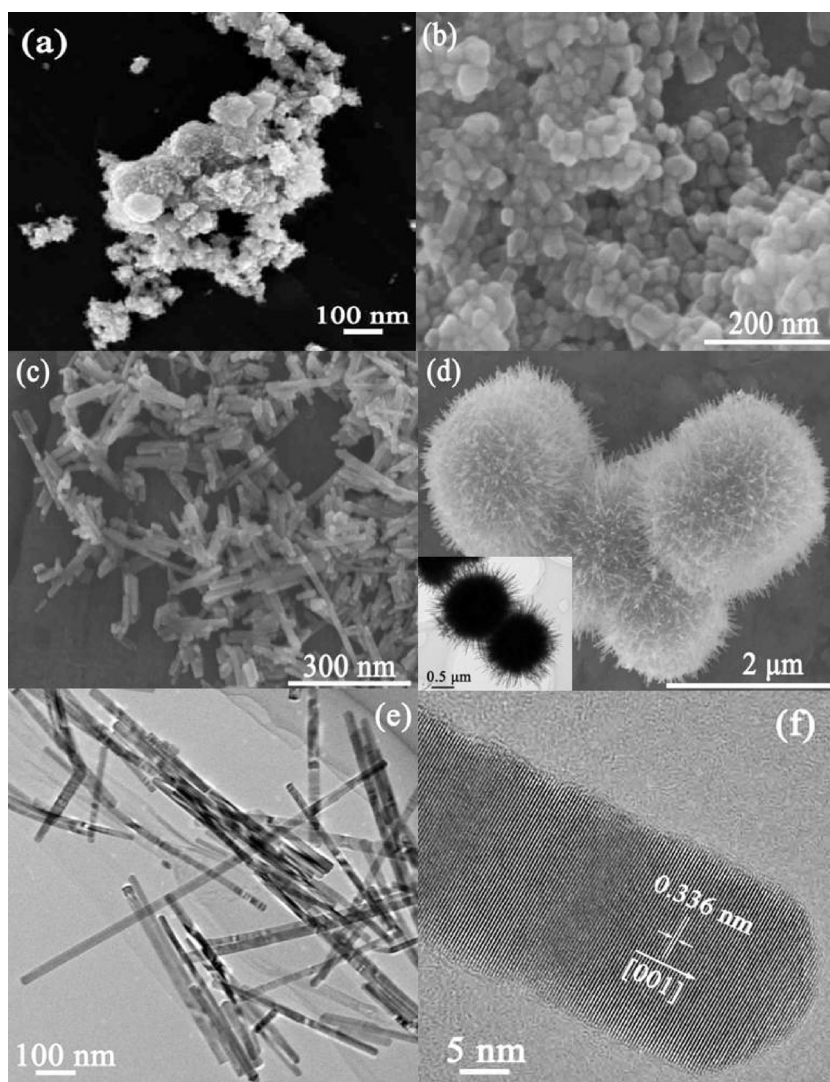


Fig. 3. FESEM images of samples A(a), B (b), C (c) and D (d); and TEM and HRTEM images of sample E (e and f).

nanoparticles and hollow spheres were formed while thiourea, TAA and L-cysteine were used as sulfur source, respectively (Fig. 2d–f). As suggested in Table 1 and Fig. 2, the samples obtained with assistance of L-cysteine as sulfur source show the highest BET surface area and quantum efficiency (QE). It is also indicated that organic solvent (i.e. EDA) is advantageous over water in terms of higher BET surface area and QE. Therefore, several typical organic solvents were studied in the following solvent-dependent synthesis, with sulfur source being fixed as L-cysteine. The details on the solvent-dependent synthesis are summarized in Table 1.

FESEM and TEM images of the A, B, C, D and E samples are shown in Fig. 3, which displays that the solvents greatly affect morphologies of the samples. The sample prepared in the presence of TEA solvent is irregular (Fig. 3a). The FESEM image of the B sample (Fig. 3b) shows that nanoparticles are obtained by using DDA as solvent. The nanoparticles have sizes ranging from 15 to 40 nm and appear to be heavily aggregated. It is interesting to note that the sample prepared in the presence of DETA solvent is composed of nanorods with lengths of ca. 60 nm–250 nm and diameters of ca. 20 nm (Fig. 3c). FESEM image (Fig. 3d) of the D sample clearly reveals that the sample prepared in EDA solution is constructed from the closely aggregation of nanorods, presenting an urchin-like structure. TEM image (the inset in Fig. 3d) of the D sample further confirms that these nanorods are highly directed to form radial

arrays from the center to the surface of spheres. Further observation shows that the length and the diameter of the constituent nanorods are ca. 1 μm and 22 nm, respectively. Moreover, the sample prepared in TEPA solution consists of many nanowires with lengths of up to 1 μm and diameters of ca. 22 nm (Fig. 3e). From the HRTEM image (Fig. 3f) of an individual nanowire, it can be observed that the space between adjacent planes is 0.336 nm, which is consistent with the interplanar distance of the (0 0 2) planes of hexagonal CdS, indicating that the nanowires grow along the c-axis direction.

3.2. X-ray diffraction study

XRD was used to investigate the crystal structures and phase compositions of the samples studied. Fig. 4a shows the XRD patterns of samples S1, S2, S3, H1, H2 and H3. The XRD patterns of samples S1, S2, and S3 are consistent with the hexagonal phase. The (1 1 0), (1 0 3) and (1 1 2) planes of wurtzite CdS are clearly distinguishable in the patterns (JCPDS No. 41-1049). In contrast, the samples H1, H2 and H3 were prepared via a hydrothermal route. For the sample H2, three distinctive reflection peaks at $2\theta = 26.5^\circ$, 44° and 52.2° are the characteristics of (1 1 1), (2 2 0) and (3 1 1) reflections of the cubic CdS (JCPDS No. 80-0019), respectively. However, a weak diffraction peak at $2\theta = 24.8^\circ$ is attributed to the hexagonal wurtzite phase of CdS. Thus, the H2 sample is a mixture of

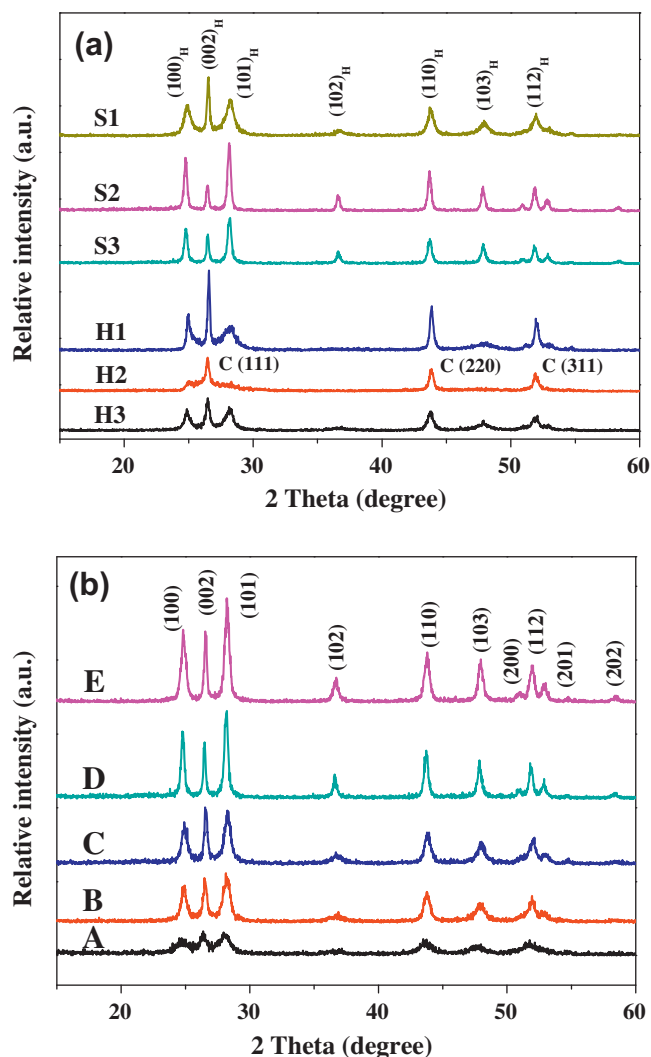


Fig. 4. XRD patterns of samples S1, S2, S3, H1, H2 and H3 (a) and samples A, B, C, D and E (b).

cubic (major) and hexagonal (minor). Further observation indicates that the (102) diffraction peak disappears and (103) diffraction peak become very weak for the H1 and H3 samples. This also indicates that the H1 and H3 samples contain cubic and hexagonal two phases. As can be seen in Fig. 4a, the samples prepared by solvothermal method show enhanced crystallinity compared to the samples prepared by hydrothermal method based on the same sulfur source.

Fig. 4b shows the XRD patterns of samples A–E. All of the diffraction peaks in this pattern can be indexed to the hexagonal phase of CdS with lattice parameters $a=4.1\text{ \AA}$ and $c=6.7\text{ \AA}$, which are well matched with literature values (JCPDS No. 41-1049). No peaks of impurities were detected, revealing the high purity of the as-synthesized products. The sample A has the hexagonal phase CdS, but poor crystallinity. Compared with that of samples B and C, the strong and sharp diffraction peaks of the XRD pattern indicate a higher crystallinity of samples D and E.

3.3. UV–vis diffuse reflection spectra

UV–vis diffuse reflectance spectra (DRS) were used to characterize the optical absorption properties of semiconductor powder materials. Fig. 5 presents a comparison of the UV–vis diffuse reflectance spectra for the samples A–E. As can be seen, the onset of the absorption edge of the samples A–D and E is at 550, 547, 532,

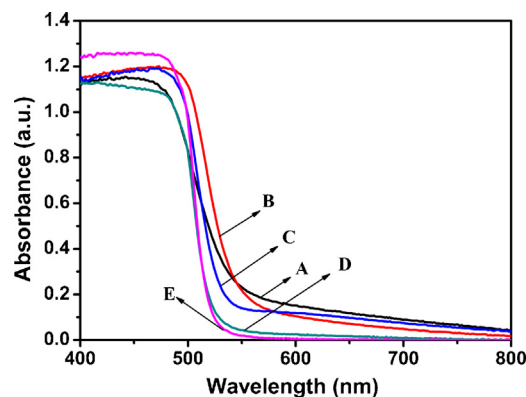


Fig. 5. UV–vis absorption spectra of the samples A, B, C, D and E.

525 and 523 nm corresponding to band gaps of 2.25, 2.27, 2.33, 2.36 and 2.37 eV, respectively. Interestingly, compared to the absorption edge of samples A and B, an obvious blue-shift in the absorption edge is observed for samples C–E. It is reasonable because different crystal facets usually own different band gap, which can be originated from different atomic configurations on each surface [19,33]. Thus, the changing morphologies and surface nanostructures may result in a widening of the band gap. Moreover, the increase in band gap could also contribute to the enhanced photocatalytic activity through changes in the redox potential for photocatalytic reactions [34].

3.4. BET

The effect of solvent on the pore structure and surface areas of as-prepared products are investigated by the nitrogen adsorption–desorption measurement. The nitrogen adsorption–desorption isotherms and the corresponding pore-size distribution curves for samples A, B and E are presented in Fig. 6. The isotherm of the sample A has two hysteresis loops, indicating bimodal pore-size distributions in the mesoporous (2–50 nm) and macroporous (>50 nm) regions. At low P/P_0 range ($0.5 < P/P_0 < 0.8$), the hysteresis loop is of type H2, suggesting the presence of narrow necks and wider bodies (ink-bottle pores). At high P/P_0 range ($0.8 < P/P_0 < 1.0$), the shape of hysteresis loop is of type H3, associated with narrow slit-shaped pores. However, the isotherm of the sample B exhibits H2 hysteresis loop associated with ink-bottle pores formed through the aggregation of particles [35]. As for sample E, the nitrogen adsorption–desorption isotherm displays hysteresis loops at high relative pressures close to unity, suggesting the formation of large mesopores and

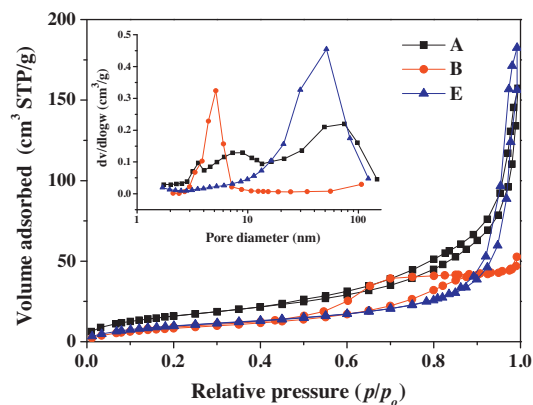


Fig. 6. Nitrogen adsorption–desorption isotherms and the corresponding pore-size distribution curves (inset) of samples A, B and E.

macropores, which can be categorized as type IV according to The International Union of Pure and Applied Chemistry (IUPAC) classification [36,37]. The shape of the hysteresis loop is of type H3 at a high relative pressure range of 0.8–1.0, indicating the presence of slit-like pores due to the aggregation of CdS nanowires. Further observations show that at low P/P_0 range (<0.2), the isotherms of samples A and E shift up compared to sample B, suggesting higher surface areas of samples A and E. The pore-size distribution curves (inset in Fig. 6) of samples A and E are very broad, further confirming the presence of mesopores and macropores [38]. Table 2 shows quantitative details on BET surface area of the samples A–E.

3.5. XPS

The chemical composition of the samples B and E were characterized by XPS. Fig. 7 displays the full XPS spectrum and high-resolution spectra of the Cd3d and S2p regions, respectively. Fig. 7a shows that no peaks of other elements except Cd, S, C, and O are observed. The C and O peaks mainly come from the contamination due to the samples exposure to air. This again indicates that the synthesized CdS samples are of high purity. As can be seen from Fig. 7b, it is obvious that the binding energy of peaks Cd 3d_{5/2} and Cd 3d_{3/2} are 405.1 and 411.9 eV, respectively. Fig. 7c displays the peaks at 161.6 eV, corresponding to the binding energy of S 2p. These results are in agreement with the reported data in the literature [38]. The Cd 3d_{5/2} and S 2p_{3/2} peak areas were determined for the quantitative elemental analysis of Cd and S in the products. An atomic ratio of approximately 1:1 is obtained, which further confirms that the products are pure CdS.

3.6. Formation mechanism of CdS nanostructures

It is well known that the morphology of materials is closely related to the growth direction of crystal. Moreover, the growth direction of crystal is determined by the surface energies (E_s) of different planes. Thus the E_s of (100) and (001) surfaces was calculated by the following formula [39]:

$$E_s = (E_{\text{slab}} - E_{\text{bulk}}) / 2A \quad (2)$$

where E_{slab} was the total energy of atom slab (containing 4 Cd atoms and 4 S atoms) of (100) or (001) surface, E_{bulk} was the total energy of $2 \times 1 \times 1$ supercell (also containing 4 Cd atoms and 4 S atoms) of bulk CdS and $2A$ was the contacting area between the atom slab and vacuum slab. The obtained E_s of (100) and (001) surfaces are 1.09 J m^{-2} and 1.64 J m^{-2} , respectively, indicating that the (001) surface is more active than the (100) surface.

According to the observed morphologies of CdS, it can be clearly seen that the (001) surfaces consist of the bottom surfaces of CdS nanorods and nanowires, while the (100) and (010) surfaces consist of the side surfaces of those. It should be noted that the (100) surface of hexagonal CdS is similar to (010) surface. As a result, the CdS crystal prefers to grow along with the direction of [001] rather than [100] and [010], which well explains the origination of one-dimensional structure of hexagonal CdS. But the CdS nanorods and nanowires exhibit different areas of (001) surfaces, due to the variation in the growths of (100) and (010) surfaces. As an oxygen-containing solvent, TEA can introduce the impurity O atoms into the lattice of CdS, which destroys the intrinsic crystal structure of CdS. Consequently, the prepared sample A is irregular (Fig. 3a).

As for the oxygen-free solvent (DDA, DETA, EDA and TEPA), the contained N atoms exhibit three-coordination, smaller than the C atoms. Hence, the N atoms in current solvents can be bonded to the exposed Cd atoms in the (100) and (010) surfaces, which can control the growths of (100) and (010) surfaces. Besides, the quantity of three-coordination N atoms (N_{3C}) in solvent molecule and the length of solvent molecule both determine the interaction between

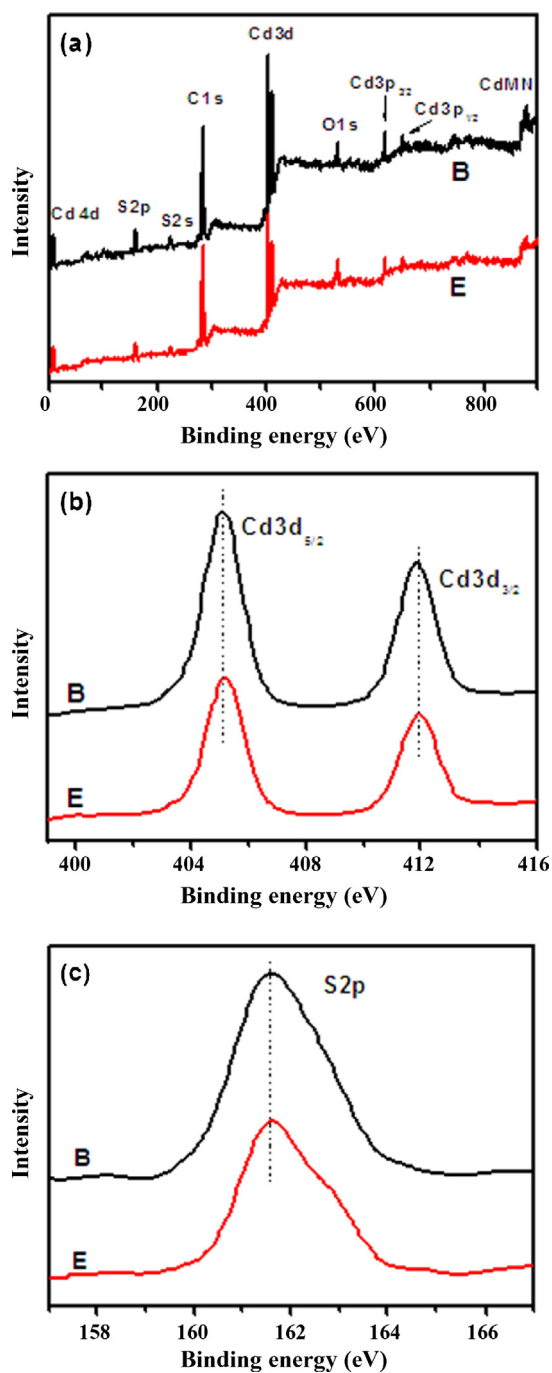


Fig. 7. XPS survey spectra (a) and high-resolution XPS spectra of Cd 3d (b) and of S 2p (c) for samples B and E.

CdS surface and solvent molecules. The DDA molecule only contains one N_{3C} atom. Thus the DDA molecule tends to be vertically adsorbed on the CdS surface, which, however, is not stable (see Fig. 8a). As a result, the DDA solvent cannot effectively limit the growths of (100) and (010) surfaces, which leads to the formation of CdS nanoparticles (Fig. 3b). However, in the TEPA molecule, the distance between adjacent N atoms is close to that between adjacent Cd atoms in (100) and (010) surfaces (see Fig. 8d). This directly enhances the interaction between TEPA molecule and CdS surface. As a result, the TEPA molecule are horizontally adsorbed on the (100) and (010) surfaces, which remarkably prevents the growths of (100) and (010) surfaces. Thus the CdS samples

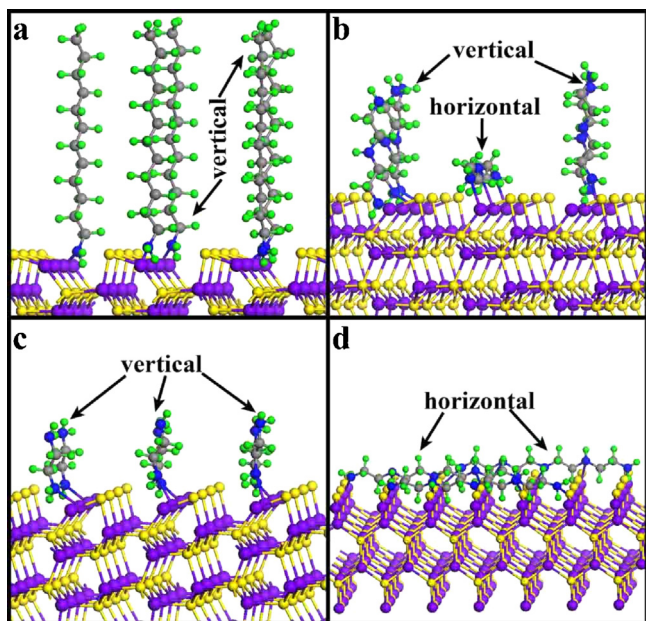


Fig. 8. The adsorption of solvent molecules on the (100) surfaces of CdS: DDA (a), DETA (b), EDA (c) and TEPA (d). The yellow, purple, gray, blue and green spheres represent S, Cd, C, N and H atoms, respectively.

prepared in the TEPA solution exhibit the wire-like morphology (Fig. 3e).

Similar to the structure of TEPA molecule, the distance between adjacent N atoms in the EDA molecule is also approximate to that between adjacent Cd atoms in (100) and (010) surfaces. But the atomic chain of EDA molecule is shorter than that of TEPA molecule. Moreover, the quantity of N_{3C} atoms in the EDA molecule is less than that in the TEPA molecule, implying the instability of horizontal adsorption of EDA molecule on the (100) and (010) surfaces. Therefore, the EDA molecule prefers to be vertically adsorbed on the (100) and (010) surfaces (see Fig. 8c). However, the adsorption of EDA molecule is slightly weaker than that of TEPA molecule. As a result, though the nanowires are prepared successfully, the formed nanowires are aggregated to constitute the sphere assemblies due to the existed interactions among nanowires (Fig. 3d).

As for the DETA molecule, the length of atomic chain and the quantity of contained N_{3C} atoms are both located between TEPA and EDA molecules. Thus the horizontal and vertical adsorptions both are possible for the DETA molecule on the (100) and (010) surfaces (see Fig. 8b). But two kinds of adsorption are weaker than the horizontal adsorption of EDA molecule and the vertical adsorption of TEPA molecule, respectively. Furthermore, the (100) and (010) surfaces of CdS nanorods tend to contact with each other. As a result, the growing rates of (100) and (010) surfaces in DETA solvent are faster than those in TEPA and EDA solvents. Thus the CdS nanorods are formed (Fig. 3c). It can be concluded that the quantity of N_{3C} atoms and the length of atomic chain of solvent molecule determine the morphology and dispersion of CdS nanowires and nanorods.

3.7. Photocatalytic activity

Photocatalytic H_2 -production activities of the prepared CdS with the different morphology were investigated under visible light irradiation using lactic acid as scavenger and 0.36 wt% Pt as co-catalyst. Fig. 9 presents a comparison of photocatalytic H_2 -production rates of samples S1, S2, S3, H1, H2, and H3. Among the three samples prepared by solvothermal methods, sample S3 exhibits the highest photocatalytic activity. Furthermore, it can be

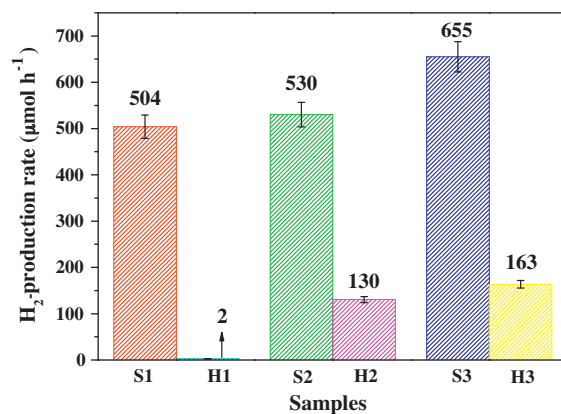


Fig. 9. Comparison of the photocatalytic H_2 -production activity of samples S1, S2, S3, H1, H2, and H3 from lactic acid aqueous solution under visible-light irradiation.

seen that samples S1, S2 and S3 show enhanced photocatalytic H_2 -production rate compared to samples H1, H2 and H3, respectively. This is attributed to the following factors: (i) the enhanced crystallinity would reduce the number of defects and the bulk electron-hole recombination; (ii) CdS photocatalyst with a hexagonal crystal structure has been found to be much more efficient in hydrogen production than CdS with a cubic crystal structure [40]; (iii) the unique 1D-based structure might facilitate the electron transport for reacting with water molecules adsorbed at the CdS surface along the 1D structure. Herein, it is reasonable to conclude that CdS 1D-based structures are beneficial to improve photocatalytic H_2 -production activity.

Fig. 10 shows a comparison of photocatalytic H_2 -production rates of samples A, B, C, D and E. It should be noted that sample A with the highest surface area shows the lowest activity resulting from the poorest crystallinity (see Fig. 4b). Thus, crystallinity seems to be more influential factor for photocatalytic activity than surface area. Our previous results also indicate that crystallinity is a more important factor than specific surface area in determining photocatalytic activity of TiO_2 [41,42]. So, it is not surprising that the sample A exhibits lowest photocatalytic H_2 -production activity due to its weakest crystallization. Additionally, the results show that the TEA solvent leads to very low photocatalytic H_2 -production activity of CdS nanocrystals compared to the DDA, EDA, DETA and TEPA solvents because of the presence of O atoms. Contrarily, CdS nanoparticles (sample B) show obvious activity with hydrogen evolution rate about $372 \mu\text{mol h}^{-1}$ due to the enhanced crystallization. The hydrogen evolution rate of CdS nanorods (sample C) is slightly

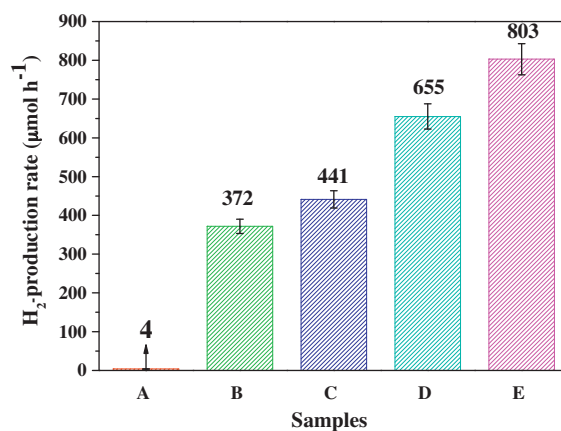


Fig. 10. Comparison of the photocatalytic H_2 -production activity of samples A, B, C, D and E from lactic acid aqueous solution under visible-light irradiation.

higher than that of CdS nanoparticles. Moreover, urchin-like CdS (sample D) exhibits high photocatalytic activity with the hydrogen evolution rate of $655 \mu\text{mol h}^{-1}$. The highest H_2 -production rate obtained from CdS nanowires (sample E) is $803 \mu\text{mol h}^{-1}$ (QE of 37.7% at 420 nm). This value exceeds that of CdS nanoparticles (sample B) by 2.2 times. The improved photocatalytic activity of CdS nanowires can be explained as follows. Firstly, CdS nanowires have high crystallinity and large specific surface areas. This also implies that the high photocatalytic activity can be associated with the balance between crystallization and specific surface areas. Secondly, the shorten distance for the photogenerated electrons and holes migrating to the reaction sites on the surface in nanowires facilitates space separation of the photogenerated electron/hole pairs. Thirdly, wider band gap corresponding to the blue shift of the absorption edge makes photogenerated electrons and holes with relatively stronger reduction or oxidation ability. Based on these results, it can be concluded that the solvent plays an important role in the morphology control and hydrogen production performance. Consequently, shape-controlled synthesis of CdS photocatalyst is an effective approach to improve its activity.

4. Conclusions

In summary, morphology-controlled CdS photocatalysts for hydrogen evolution were synthesized by a facile solvothermal method by adjusting the sulfur source and solvent. The solvothermal products had high crystallinity and characteristic morphologies with high potential for catalytic applications. The highest visible-light photocatalytic H_2 -production rate for CdS nanowires ($803 \mu\text{mol h}^{-1}$) prepared in tetraethylenepentamine (TEPA) solvent was approximately 2.2 times higher than that of CdS nanoparticles prepared in dodecylamine (DDA) solvent. It can be concluded that the small diameter of nanowire structure make it easy for photogenerated electrons and holes to migrate to the surface active sites. Hence, the nature of solvent has great influence on the morphology and photocatalytic H_2 -production activity of CdS photocatalyst. It was concluded that the quantity of N_3C atoms and the length of atomic chain of solvent molecule determine the morphology and dispersion of CdS nanowires and nanorods. The morphology and crystal structure of CdS photocatalyst are key factors for achieving highly efficient photocatalytic hydrogen production under visible light.

Acknowledgements

This work was partially supported by the 973 program (2013CB632402), NSFC (51320105001, 51372190 and 51272199), Fundamental Research Funds for the Central Universities (WUT:

2013-VII-030) and Self-determined and Innovative Research Funds of SKLWUT (2013-ZD-1).

References

- [1] A. Fujishima, K. Honda, *Nature* 238 (1972) 37.
- [2] Q.J. Xiang, J.G. Yu, *J. Phys. Chem. Lett.* 4 (2013) 753.
- [3] J.H. Park, S. Kim, A.J. Bard, *Nano Lett.* 6 (2006) 24.
- [4] I. Tsuji, H. Kato, H. Kobayashi, A. Kudo, *J. Am. Chem. Soc.* 126 (2004) 13406.
- [5] A. Kudo, Y. Miseki, *Chem. Soc. Rev.* 38 (2009) 253.
- [6] Q. Li, B. Guo, J.G. Yu, J.R. Ran, B. Zhang, H. Yan, J.R. Gong, *J. Am. Chem. Soc.* 133 (2011) 10878.
- [7] G.K. Mor, H.E. Prakasham, O.K. Varghese, K. Shankar, C.A. Grimes, *Nano Lett.* 7 (2007) 2356.
- [8] Q. Xiang, B. Cheng, J. Yu, *Appl. Catal. B* 138 (2013) 299.
- [9] Q. Li, H. Meng, J. Yu, W. Xiao, *Chem. Eur. J.* 20 (2014) 1176.
- [10] J. Yu, J. Jin, B. Cheng, M. Jaroniec, *J. Mater. Chem. A* 2 (2014) 3407.
- [11] J. Jin, J. Yu, G. Liu, P.K. Wong, *J. Mater. Chem. A* 1 (2013) 10927.
- [12] H.G. Yang, C.H. Sun, S.Z. Qiao, J. Zou, G. Liu, S.C. Smith, H.M. Cheng, G.Q. Lu, *Nature* 453 (2008) 638.
- [13] J.G. Yu, P. Zhou, Q. Li, *Phys. Chem. Chem. Phys.* 15 (2013) 12040.
- [14] H.G. Yang, G. Liu, S.Z. Qiao, C.H. Sun, Y.G. Jin, S.C. Smith, J. Zou, H.M. Cheng, G.Q. Lu, *J. Am. Chem. Soc.* 131 (2009) 4078.
- [15] P. Zhou, J.G. Yu, Y.X. Wang, *Appl. Catal. B* 142–143 (2013) 45.
- [16] Y. Li, L. Tang, S. Peng, Z. Li, G. Lu, *CrystEngComm* 14 (2012) 6974.
- [17] L. Qi, J. Yu, M. Jaroniec, *Phys. Chem. Chem. Phys.* 13 (2011) 8915.
- [18] M. Ashokkumar, *Int. J. Hydrogen Energy* 23 (1998) 427.
- [19] C. Li, L.J. Han, R. Liu, H. Li, S. Zhang, G. Zhang, *J. Mater. Chem.* 22 (2012) 23815.
- [20] N. Bao, L. Shen, T. Takata, K. Domen, *Chem. Mater.* 20 (2008) 110.
- [21] L. Shen, N. Bao, P.E. Prevelige, A. Gupta, *J. Phys. Chem. C* 114 (2010) 2551.
- [22] J.G. Yu, Y.F. Yu, B. Cheng, *RSC Adv.* 2 (2012) 11829.
- [23] D. Jing, L. Guo, *J. Phys. Chem. B* 110 (2006) 11139.
- [24] M. Muruganandham, Y. Kusumoto, C. Okamoto, A. Muruganandham, M. Abdulla-Al-Mamun, B. Ahmmad, *J. Phys. Chem. C* 113 (2009) 19506.
- [25] C.J. Barrelet, Y. Wu, D.C. Bell, C.M. Lieber, *J. Am. Chem. Soc.* 125 (2003) 11498.
- [26] C.C. Chen, C.Y. Chao, Z.H. Lang, *Chem. Mater.* 12 (2000) 1516.
- [27] M. Zhang, T. Zhai, X. Wang, Y. Ma, J. Yao, *Cryst. Growth Des.* 10 (2010) 1201.
- [28] T. Zhai, X. Fang, Y. Bando, Q. Liao, X. Xu, H. Zeng, Y. Ma, J. Yao, D. Golberg, *ACS Nano* 3 (2009) 949.
- [29] Y. Liang, C. Zhen, D. Zou, D. Xu, *J. Am. Chem. Soc.* 126 (2004) 16338.
- [30] Y. Li, Y. Hu, S. Peng, G. Lu, S. Li, *J. Phys. Chem. C* 113 (2009) 9352.
- [31] S. Xiong, B. Xi, C. Wang, G. Zou, L. Fei, W.Y. Wang, Qian, *Chem. Eur. J.* 13 (2007) 3076.
- [32] J.S. Jang, U.A. Joshi, J.S. Lee, *J. Phys. Chem. C* 111 (2007) 13280.
- [33] G. Liu, C. Sun, H.G. Yang, S.C. Smith, L. Wang, G.Q.M. Lu, H.M. Cheng, *Chem. Commun.* 46 (2010) 755.
- [34] Q. Li, H. Meng, P. Zhou, Y. Zheng, J. Wang, J. Yu, J.R. Gong, *ACS Catal.* 3 (2013) 882.
- [35] R. Chen, J. Yu, W. Xiao, *J. Mater. Chem. A* 1 (2013) 11682.
- [36] L. Nie, A. Meng, J. Yu, M. Jaroniec, *Sci. Rep.* 3 (2013) 3215.
- [37] K. Singh, D. Everett, R. Haul, L. Moscou, R. Pierotti, J. Rouquerol, T. Siemieniowska, *Pure Appl. Chem.* 57 (1985) 603.
- [38] D. Wang, D. Li, L. Guo, F. Fu, Z. Zhang, Q. Wei, *J. Phys. Chem. C* 113 (2009) 984.
- [39] H.Z. Liu, M.T. Zhao, Y.K. Lei, C.X. Pan, W. Xiao, *Comput. Mater. Sci.* 51 (2012) 389.
- [40] M. Matsumura, S. Furukawa, Y. Saho, H. Tsubomura, *J. Phys. Chem. C* 89 (1985) 1327.
- [41] J. Yu, W. Wang, B. Cheng, B. Huang, X. Zhang, *Res. Chem. Intermediates* 35 (2009) 653.
- [42] W. Wang, J. Yu, Q. Xiang, B. Cheng, *Appl. Catal. B* 119 (2012) 109.